IOP Publishing Physics in Medicine and Biology

Phys. Med. Biol. **52** (2007) 4121–4136 doi:10.1088/0031-9155/52/14/007

Interstitial fluid pressure in soft tissue as a result of an externally applied contact pressure

A L Darling[1], P K Yalavarthy[1], M M Doyley[1], H Dehghani[1,2] and B W Pogue[1]

[1] Thayer School of Engineering, Dartmouth College, Hanover NH 03755, USA
[2] University of Exeter, Stocker Road, Exeter EX4 4QL, UK

E-mail: brian.w.pogue@dartmouth.edu

Received 12 January 2007, in final form 15 March 2007
Published 13 June 2007
Online at stacks.iop.org/PMB/52/4121

Abstract

Manipulation of interstitial fluid pressure (IFP) has a clinical potential when used in conjunction with near-infrared spectroscopy for the detection of breast cancer. In order to better interpret how the applied pressure alters the vascular space and interstitial water volumes in breast tissue, a study on tissue-mimicking, gelatin phantoms was carried out to mimic the translation of external force into internal pressures. A complete set of three-dimensional (3D) pressure maps were obtained for the interior volumes of phantoms as an external force of 10 mmHg was applied, using mixtures of elastic moduli 19 and 33 kPa to simulate adipose and fibroglandular values of breast tissue. Corresponding linear elastic finite element analysis (FEA) cases were formulated. Shear stress, nonlinear mechanical properties, gravity and tissue geometry were all observed to contribute to internal pressure distribution, with surface shear stresses increasing internal pressures near the surface to greater than twice the applied external pressure. Average pressures by depth were predicted by the linear elastic FEA models. FEA models were run for cases mimicking a 93 kPa tumor inclusion within regions of adipose, fibroglandular tissue, and a composite of the two tissue types to illustrate the localized high fluid pressures caused by a tumor when an external force is applied. The conclusion was that external contact forces can generate potentially clinically useful fluid pressure magnitudes in regions of sharp effective elastic modulus gradients, such as tumor boundaries.

1. Introduction

Manipulating interstitial fluid pressure (IFP) could potentially create transient optical effects in soft tissue to increase the detectability of inhomogeneities such as tumors. In particular,

near-infrared (NIR) imaging of tissues has been shown to be sensitive to transient microvascular phenomena involving oxygen saturation, from time-varying vascular changes in hemoglobin state (Barbour *et al* 2001) to local metabolism in brain function (Boas and Dale 2005). Other work in applied pressure during imaging has demonstrated NIR signal changes in response to external compression (Jiang *et al* 2003, Carp *et al* 2006). While it is known that external forces can increase IFP, the relationship of the applied mechanical surface pressure to internal hydrostatic pressure in a nonlinear, porous, viscoelastic solid such as soft tissue is a complex problem that evades an analytical solution. To explore this relationship and the possibility of using IFP in cancer detection, a series of phantom and finite element studies were performed. Fluid pressure measurements were taken in gelatin phantoms of equivalent elastic moduli to tissues of the breast, using an embedded pressure transducer and a compression tester to put load on the phantoms. These measurements and corresponding simulations were used to predict the changes which should be observed in human breast tissues under externally applied compression.

IFP may be defined as the hydrostatic pressure of liquid in small pores within a matrix of cells, proteins and microvessels that make up the tissue, and models of IFP must take into account both fluid and solid properties (Guyton *et al* 1971). This hydrostatic pressure is maintained in a dynamic environment by fluid transfer between the vessels and tissue governed by Starling forces, the contractile forces of cells within the tissue, the microanatomy of the tissue, and the complex mechanical properties of the tissue as a whole (Heldin *et al* 2004). The tissue surrounding the pores is not truly linear elastic and may be more accurately described as nonlinear, anisotropic, hyperelastic and viscoelastic, but analytical solutions for such problems are usually not possible, so linear elastic approximations are used (Bilston 2002). Rigorous experimental analysis has shown that such linear elastic approximations are sufficient to predict stress–strain relationships within soft tissue for small strains (Krouskop *et al* 1998). Furthermore, IFP may be directly altered by applying external force to the tissue, i.e. applying a blood pressure cuff to a patient's arm to collapse blood vessels present there. Lesser surface pressure could be utilized to collapse microvessels selectively, resulting in NIR detectable changes in water volume and oxygenation.

It has been observed that, under normal physiological conditions, the IFP is significantly greater in tumors than in surrounding tissues (Boucher and Jain 1992, Heldin *et al* 2004, Nathan *et al* 2005). There are several reports showing that tumors tend to possess greater stiffness than normal tissue and that the tumor size correlates to increasing IFP (Stur *et al* 2003, Krouskop *et al* 1998, Gutmann *et al* 1992). If localized changes in mechanical properties can increase the hydrostatic pressure beyond that of the surrounding tissue when an external force is applied, then methods that detect changes in interstitial fluid pressure indirectly (deoxygenation rate, reduced vascular volume, etc) may be used to detect such regions of local variance, i.e. tumors. For instance, in the case of near-infrared spectral detection, absorbing and scattering coefficients of internal tissues were found to change when the force was applied to the exterior of breast tissue or arm tissue (Jiang *et al* 2003, Carp *et al* 2006). Biological tissues with cancerous tumors may be thought of as heterogeneously elastic materials containing harder/softer masses embedded in the matrices (Liu *et al* 2003). If the pressure can be altered locally in regions of different mechanical properties, it offers an opportunity for cancer detection and/or characterization.

Soft tissue mechanical properties are complex; they are frequently nonlinear and viscoelastic (Dehghani *et al* 2004). It is accepted, though, that for small strain ranges and with the assumption that tissue is incompressible (Poisson's ratio ~ 0.5), linear elastic theory can approximate their behavior (Erkamp *et al* 2004, Liu *et al* 2003, Azar *et al* 2001). Equations governing small strain pressure and fluid migration are considered acceptable on the order of

10 mmHg applied stress (Netti *et al* 1997). For larger strains, soft tissues follow a nonlinear J-shaped stress–strain curve similar to what is observed in elastomers such as rubber. As greater force is applied to such materials, they become stiffer (Gordon 1980). The effective elastic modulus at 40% strain could be several times greater than that at 10% strain. For this reason, it is frequently useful to collect a soft tissue sample's stress–strain curve from zero strain up to failure in order to fully characterize an effective elastic modulus.

With the goal of creating phantoms for breast tissue, the mechanical properties of natural breast tissue were considered and suitable materials to duplicate them were created. Gelatin is a very convenient material, as it requires only a mixture with water, heating and cooling to form in a mold. Varying the concentration in relation to water can adjust the mechanical properties to coincide with those seen in adipose and fibroglandular tissue of the breast (Greenleaf *et al* 2003, Erkamp *et al* 2004). Data collected by Krouskop *et al* (1998) show breast tissue elastic moduli of 19 ± 7 for fatty breast tissue, 33 ± 11 for glandular breast tissue, 107 ± 31 for fibrous tissue, 25 ± 4 for ductal carcinoma and 93 ± 33 for invasive and infiltrating ductal carcinoma. The initial part of this study focused upon defining gelatin phantoms of correct concentration to emulate the specific mechanical properties of adipose and fibroglandular breast tissues.

2. Modeling

To calculate IFP within a region of tissue, one must consider the system as a fluid cavity within a solid material. In tissue at the macroscopic level, this solid material is approximated as a poroelastic substrate, in which the internal fluid pressure is governed by the displacement field, and the displacement field varies by time at a rate determined by fluid permeability of the porous solid and the permeability of the capillary and lymphatic walls within the tissue (Leiderman *et al* 2006, Netti *et al* 1997). The relationship between stress, pressure and displacement field is described as

$$\sigma_t = -pI + \lambda \nabla \cdot uI + 2\mu \nabla^{\mathrm{Sym}} u, \tag{1}$$

where σ_t is the total stress in the interstitium at the macroscopic level, p is interstitial fluid pressure, I is the identity matrix, λ and μ are the solid matrix Lamé constant, u is the displacement field and $\nabla^{\mathrm{Sym}} u$ is equal to the infinitesimal strain tensor ε. This equation is appropriate for linear elastic and poroelastic solid materials, as fluid migration is taken into account in the displacement field as

$$\nabla \cdot \dot{u} - \nabla \cdot [\kappa \nabla p] + \chi p = 0, \tag{2}$$

where κ is the interstitial permeability, $\dot{u}$ is the solid phase velocity, and χ is the average microfiltration rate over capillary and lymphatic walls. In a gelatin phantom model, there is no fluid migration due to vessels, the interstitial permeability is very low, and creep is not observable in the 15 to 30 s necessary to take a pressure measurement. Therefore, κ, χ and $\dot{u}$ are essentially zero when steady compression is applied to a gelatin phantom. Fluid migration parameters are of varying magnitudes by tissue type and vascularization, very low in poorly vascularized adipose tissue and high in porous tissue such as the brain.

At the level of the microscopic fluid inclusion, equation (1) is equivalent to an established deformation law for Newtonian viscous fluid given by Stokes and described by equations (3)–(5) (Stokes 1845, White 1991):

$$\tau_{ij} = -p\delta_{ij} + \mu \left(\frac{\partial v_i}{\partial x_j} + \frac{\partial v_j}{\partial x_i} \right) + \delta_{ij} \lambda \operatorname{div} V, \tag{3}$$

where τ_{ij} is the surface stress on the faces of a fluid element, v is the fluid velocity, and $\frac{\partial v}{\partial x}$ is the fluid strain rate. In this context, the strain rate is interchangeable with strain $\varepsilon_{ij} = \frac{\partial u_i}{\partial x_j}$ as we are interested in the compression of a fluid between two steady states, i.e. time is equal to zero or one, so velocity equals displacement. By summing both sides of equation (3) for all indices $i = j$, a relationship can be determined for thermodynamic pressure p, and the compression of the fluid, div V, as shown in equation (4). This may, in turn, be rewritten as equation (5) by substituting trace of fluid strain rate with divergence of volume, a kinematic relationship (White 1991):

$$(\tau_{xx} + \tau_{yy} + \tau_{zz}) = -3p + 2\mu(\varepsilon_{xx} + \varepsilon_{yy} + \varepsilon_{zz}) + \lambda \,\mathrm{div}\, V \tag{4}$$

$$\bar{p} = -\tfrac{1}{3}(\tau_{xx} + \tau_{yy} + \tau_{zz}) = p - \left(\lambda + \tfrac{2}{3}\mu\right)\mathrm{div}\, V, \tag{5}$$

where $\bar{p}$ is defined as the mechanical pressure. Equation (5) illustrates that mechanical and thermodynamic pressure are distinct, and that thermodynamic pressure inside a fluid will not equal the force applied to the exterior surface, if there is compression of the fluid. Further, fluid inclusions throughout a solid will have varying pressures if there is any stress inhomogeneity.

For the approximation of equation (5) to be valid, the material itself must be isotropic, and the material specific properties of λ and μ, also known as the coefficient of bulk viscosity and the first coefficient of viscosity, must be known. These properties can be highly variable, and in this study, the coefficient for divergence of volume was instead found by normalizing a material-specific constant to the experimental data.

$$p = -\tfrac{1}{3}\mathrm{tr}(\tau_{ij}) + C \cdot \mathrm{tr}(\varepsilon_{ij}) \tag{6}$$

where C, a viscosity correction coefficient, equivalent to $(\lambda + \frac{2}{3}\mu)$ in equation (5) is difficult to characterize, and is usually dealt with by assuming it to be zero (Stokes 1845) or assuming the material to be truly incompressible such that the divergence of volume is zero (White 1991). The values of λ and μ may be calculated from elastic modulus and Poisson's ratio, but small errors on those values can result in very large errors in the calculated pressure. For the purposes of this study, this viscosity correction coefficient was determined from the gelatin phantoms, in a manner described in materials and methods.

Using equation (6), it should be possible to calculate regional hydrostatic pressure within a linear elastic material, provided local stress and strain can be calculated from bulk mechanical properties and a viscosity correction coefficient, C, can be determined. With instantaneous knowledge of a displacement field, this equation would also apply to transient interstitial fluid pressures with fluid migration using equations (1) and (2) to determine macroscopic stress and displacement.

3. Materials and methods

A series of experiments was performed in which gelatin, a material possessing elastic properties similar to breast tissue, was compressed under static loading, and internal pressures were measured using a small catheter pressure transducer. These pressure maps were then compared to a finite element solution in which a linear elastic model was exposed to plane strain loading conditions, and the fluid pressure within each element was estimated as a function of the mean of normal stresses, the trace of strain and a material-dependent viscosity correction coefficient. Finally, to illustrate the utility of IFP manipulation in clinical applications, the

FEM analysis was performed on heterogeneous material models of breast tissue, consisting of combinations of adipose tissue, fibroglandular tissue and infiltrating ductal carcinoma-like inclusions.

The goal of the experiments was to determine the distribution of fluid pressure within 3D gelatin phantoms of equivalent mechanical properties to the tissues found in the human breast under light external contact pressure. To this end, samples were compressed until they yielded using standard compression testing, and a relationship for effective linear elastic modulus versus gelatin composition was developed. Larger phantoms of equivalent elastic modulus to adipose and fibroglandular breast tissue were then constructed and subjected to 10 mmHg external contact pressure, while measuring internal fluid pressure at 30 different locations within each sample. Pressure maps were obtained for multiple conditions, including a 50 mm cube of adipose-simulating gelatin, studied both with and without surface lubrication; a 100 mm cube of adipose-simulating gelatin without surface lubrication, and a 50 mm cube of fibroglandular tissue-simulating gelatin without surface lubrication. The point of studying samples with and without surface lubrication was to understand the influence of surface shear stresses upon the resulting internal pressure distributions. Each of these conditions was duplicated in a simplified computational model of fluid pressure within a linear elastic solid.

3.1. Characterization of tissue-simulating phantoms

To construct phantoms of elastic modulus equivalent to either fatty (adipose) or fibroglandular breast tissue, 19 kPa or 33 kPa, respectively, three concentrations of gelatin were prepared and compression tested to determine the elastic modulus. Three samples each of 10%, 15% and 20% gelatin by weight were constructed. Samples were prepared by adding 20, 30 and 40 g of 175 bloom porcine skin derived gelatin (Sigma Aldrich, St. Louis, MO) to 180, 170 and 160 g of distilled water, respectively. Mixtures were heated to approximately 55 °C, allowed to cool to 35 °C, and were then placed in a vaseline-coated cylindrical mold, 45 mm in diameter and 45 mm in height. The samples were then cooled at 4 °C for 2 h and immediately stored in vegetable oil until mechanical testing.

All mechanical testing was performed on an Instron 4469 device (Instron Limited, Canton, MA), equipped with a 5 kN load cell 2525-805, which was certified accurate to within 1.25 N. The cylindrical samples were compressed using standard compression platens, at a rate of 6 mm min^{-1} with no preload. All nine samples were compressed to failure, and stress–strain curves were compiled. The effective elastic modulus was estimated as the slope of the stress–strain curve between 0.25 and 4 kPa of the applied external stress. To obtain desired concentrations for 19 and 33 kPa gelatin, the effective elastic modulus was compared to concentration, and a relationship was determined.

3.2. Pressure mapping of phantoms under external loading

Fluid pressure mapping was performed by applying a 10 mmHg external load to the cube samples of gelatin while taking internal pressure measurements at 30 points within each sample, as diagrammed in figure 1. The pressure mapping process consisted of placing the gelatin cube sample in the Instron 4469 equipped with 5 kN load cell, and applying a set amount of force equivalent to 10 mmHg, dependent upon the surface area of the cube. For each of the 30 points within the sample, a SmartWire Pressure Guide Wire connected to a Wavemap Pressure System (Volcano Corporation, Rancho Cordova, CA), was dipped in vegetable oil and then inserted into the gelatin cube. The probe was inserted through a 5 in. long 20 ga.

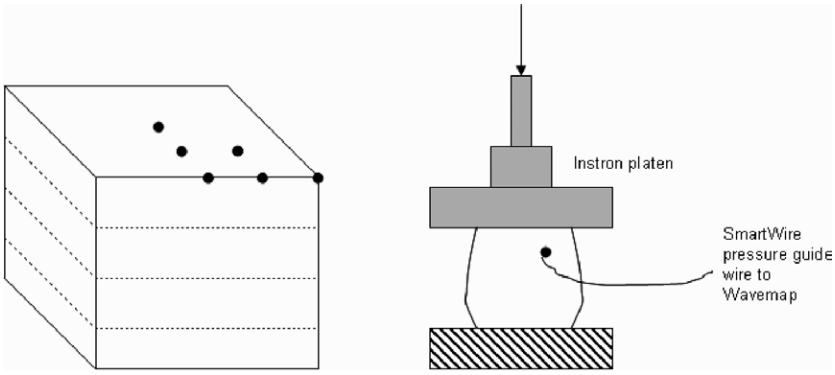

Figure 1. A diagram of pressure measurement within the phantoms. Each circle denotes a point of measurement, and the dashed lines indicate the planes of measurement, in addition to the upper and lower surfaces. Six points of measurement were taken in the displayed triangular pattern at each of the planes of measurement for a total of 30 measurements from 1/8th of the cube.

syringe needle. Vegetable oil was selected as the fluid medium in which to measure pressure change, as water would have altered the composition of the gelatin samples through osmosis. The pressure readout was set to zero, and a load equivalent to 10 mmHg was applied (3.3 N for 50 mm cubes, 13.2 N for 100 mm cubes). It was noted that measuring the pressure change when the load was removed resulted in more repeatable measurements than measuring the pressure change when the load was applied. The range of the SmartWire/Wavemap system, normally intended for blood pressure, is -30 to 100 mmHg with a listed accuracy of ± 3 mmHg, but calibration tests using a 50 mL graduated cylinder of vegetable oil demonstrated a repeatable accuracy on the scale of ± 1 mmHg.

Four material and loading conditions were used. The specimens were a 50 mm cube of adipose-simulating ($E = 19$ kPa) gelatin with the upper and lower surfaces in contact with the steel platens without lubrication, a 100 mm cube of adipose-simulating gelatin without lubrication, a 50 mm cube of fibroglandular-tissue-simulating ($E = 33$ kPa) gelatin without lubrication and a 50 mm cube of adipose-simulating gelatin lubricated on the upper and lower surface with vegetable oil. Based upon the results of the mechanical testing of gelatins of differing compositions, the adipose-simulating gelatin was prepared as 10.77% gelatin by weight, and the fibroglandular-tissue-simulating tissue was simulated as 13.93% gelatin by weight. All of the cubes were subjected to 10 mmHg loading along the vertical axis. Prior to pressure mapping, the displacement of the cube sample under the appropriate pressure was noted. With every cube, a cylindrical sample was prepared from the same gelatin batch, and mechanical properties were obtained through compression testing.

The 30 points of pressure mapping for each cubic sample were selected from 1/8th of each cube, assuming two planes of symmetry. Six measurements were taken from each of five planes in the z-axis: roughly one mm below the upper surface of the sample, 25% distance from the upper surface, 50% distance from the upper surface, 75% from the upper surface, and roughly 1 mm above the lower surface. The samples were loaded and unloaded separately for each pressure measurement. It is noteworthy that the pressure measurements are actually the change in pressure between an unloaded and loaded state, rather than a measure of absolute internal fluid pressure, as even in the unloaded state, there is some internal fluid pressure due to gravity.

3.3. Computational modeling of fluid pressure within a linear elastic solid

Pressure was modeled using static explicit structural analysis in ANSYS ED 10.0 finite element analysis software (ANSYS Inc., Canonburg, PA). The mesh was composed of type 45 8-node structural brick elements, with a nodal stress output and in a cubic configuration. In this element type, each node possesses three translational degrees of freedom. The models were formulated as either 50 mm or 100 mm cubic volumes with displacement boundary conditions placed on the upper and lower surfaces. Meshes consisted of 512 elements 6.25 or 12.5 mm on edge depending upon the size of the model and 729 nodes. Gravity was simulated by establishing a global inertia field of 9.81 m s^{-2} and a material density of 1 g cm^{-3}.

Four separate simulations were run, that of a 50 mm adipose-simulating phantom with shear forces present, a 100 mm adipose-simulating phantom with shear forces present, a 50 mm fibroglandular-tissue-simulating phantom with shear forces present, and a 50 mm adipose-simulating phantom without shear forces present. The phantom materials were modeled as isotropic linear elastic materials with an elastic modulus of 19 kPa for the fat-simulating phantom, 33 kPa for the fibroglandular-tissue-simulating phantom and Poisson's ratio of 0.495. A vertical displacement was applied to the upper surface nodes equivalent to the displacement observed in the analogous experimental model. The lower surface nodes were subjected to a displacement condition of $u_z = 0$. For the simulations of unlubricated conditions in which the shear stress was a major contributing force, the lateral displacements, u_x and u_y, of the nodes on the upper and lower surface were set to zero. For the simulation of the lubricated phantom, no u_x or u_y displacement constraints were placed. For each case, a separate model was created in which only the gravity body force was applied, along with the appropriate lower surface displacement conditions. This created an estimate of the pressures within each model in the unloaded state.

In all cases, the local hydrostatic pressure was estimated as the negative mean of the normal nodal stresses plus the trace of strain multiplied by a viscosity correction coefficient, determined by normalizing the experimental phantom measurements. This viscosity correction factor was obtained by solving equation (6) for C, setting pressure as the maximum measured pressure on the upper surface of the equivalent phantom and using stresses and strains from the analogous point on the FEM model. FEM pressures were taken as the difference between pressure in the loaded model and the unloaded (body force only) model. As the viscosity correction coefficient will change as mechanical properties change, and gelatin is a nonlinearly hyperelastic solid, separate correction coefficients were found to be needed for the loaded and unloaded states. The correction coefficient for the loaded condition was determined by normalizing the highest pressure point observed on the upper surface of the phantom of equivalent loading conditions, and the correction coefficient for the unloaded condition was determined by normalizing the average pressure of the lower surface in the loaded condition, as the pressures on the lower surface were nearly homogenous.

Four cases of heterogeneous material were also simulated using finite element analysis, to demonstrate biologically relevant applications. A 50 mm cube adipose model with a 93 kPa inclusion was simulated using the viscosity terms from the earlier analysis of the 19 kPa model. The inclusion consisted of a 12.5 mm cube located midway along the z-axis of the cube but offset 12.5 mm from the center in the x and y axes. The inclusion was assumed to have the same viscosity terms as the surrounding material. A similar model was performed for fibroglandular tissue, 33 kPa, with an inclusion. The third heterogeneous model was a more anatomic pattern with a 12.5 mm thick layer of adipose, 19 kPa, above and below a 25 mm thick fibroglandular layer, 33 kPa. The final model was a similar adipose/fibroglandular

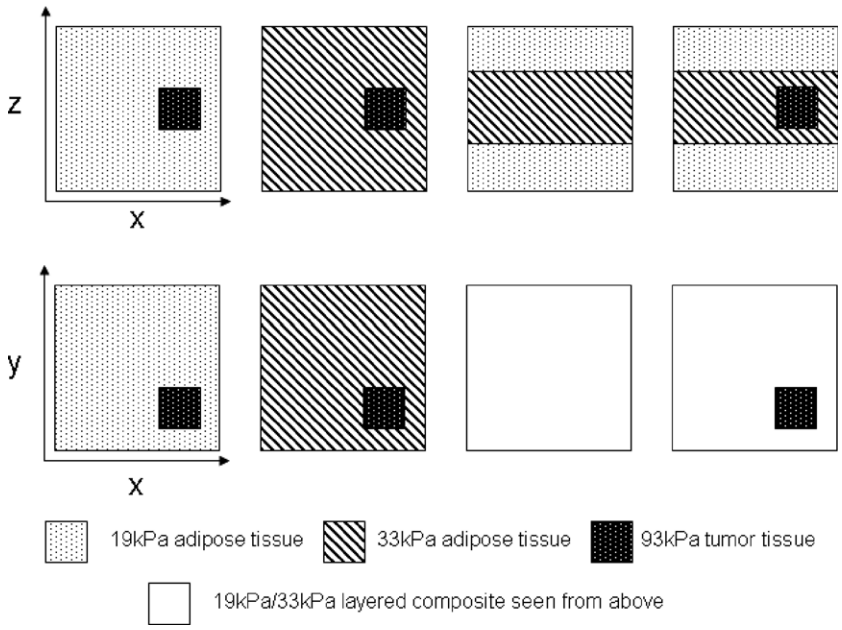

Figure 2. A schematic of the four heterogeneous models examined by FEA, as viewed from the side (top row) and from above (bottom row). From left to right, the models include adipose tissue with a 93 kPa inclusion, fibroglandular tissue with a 93 kPa inclusion, a composite of adipose and glandular tissue and a composite of adipose and glandular tissue with a 93 kPa inclusion. The inclusions were located in the middle of their sample vertically and offset to one corner in the x and y directions.

composite with a 93 kPa inclusion. Schematics of these heterogeneous cases are displayed in figure 2.

4. Results

4.1. Mechanical testing of gelatin

Mechanical testing of gelatins of differing compositions showed the J-shaped stress–strain curve typical of elastomers and soft biological tissues. Displayed in figure 3 are the stress–strain curves of one set of 10%, 15% and 20% by weight gelatin samples ($n = 1$). The elastic modulus of the range of 0.25 kPa–4 kPa applied stress was determined as the slope of the stress–strain curve within this region of stress. The relationship between gelatin concentration and effective elastic modulus suggests a trend line of $E = 4.44x - 28.79$, with E being the effective elastic modulus and x being percentage gelatin by weight. On this basis, the gelatin weight percentage selected to simulate fatty tissue was 10.77%, and the percentage selected to simulate fibroglandular tissue ($E = 33$ kPa) was 13.93%.

4.2. Phantom and FEA pressure maps

The pressure maps for both the phantom measurements and the equivalent FEA cases are shown in figure 4. Comparison of the models shows a close correlation between the experimental data and the model with linear elastic assumptions, with the exception of the lubricated

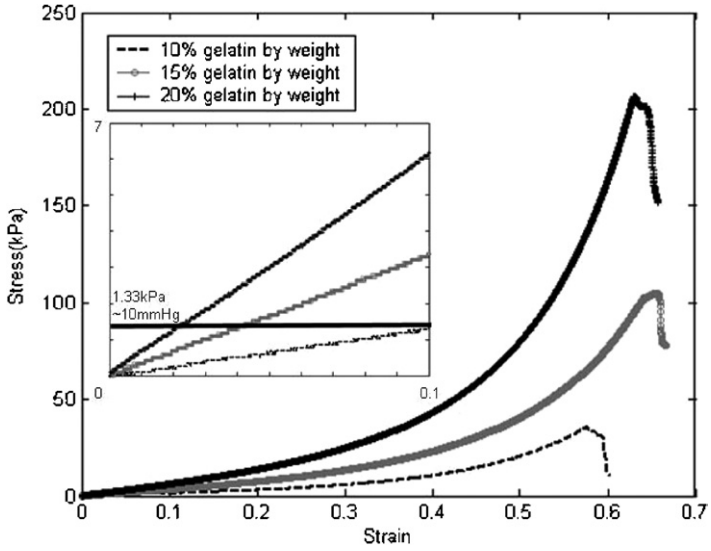

Figure 3. Compression test results for 10%, 15% and 20% by weight gelatin phantoms. The inset shows the near-linear region, with 1.33 kPa (10 mmHg) marked with a horizontal line.

phantom as compared to the FEA model with no surface shear stress. In general, the phantom measurements exhibited higher pressures along the vertical centerline than were observed in the FEA models.

The 50 mm adipose-simulating cube under 10 mmHg external pressure demonstrated a heterogeneous and asymmetric pressure distribution. The upper surface experienced high internal fluid pressures at the edges of the cube, while the lower surface experienced comparatively uniform pressures on the scale of 6 mmHg. Displacement of the cube was 5.35 mm, and the measured effective elastic modulus, as determined from a cylindrical template made from the same gelatin batch, was 18 kPa. The FEA pressure map for an equivalent model showed a striking similarity in pressure distribution, although the phantom centroid possessed a pressure peak not observed in the FEA model.

The pressure map of the fibroglandular-tissue-simulating cube revealed a similar pattern of high peripheral pressures at the topmost face, but the magnitude of the pressure was significantly higher, with a maximum value of 22.5 mmHg, compared to the maximum value of 13 mmHg observed in the fat-simulating cube of similar dimensions. In addition, there were local pressure peaks in the middle of the planes 50% and 100% distant from the top surface. The displacement observed below 10 mmHg external pressure was 2.85 mm, and the measured elastic modulus of the gelatin batch was 26 kPa. The FEA model demonstrated a similar high pressure at the upper surface, followed by a sudden drop-off in pressure at lower levels.

The 100 mm adipose-simulating cube phantom demonstrated a similar vertical asymmetry, with high peripheral pressures on the upper surface, and more uniform pressures on the bottom surface. On both the upper and lower surfaces, there was an increased pressure at the center of the face. Pressures in the middle of the sample, vertically, were somewhat lower and more diffuse than those observed in the 50 mm cube of similar mechanical properties and were closer to the corresponding FEA model. The observed displacement was 6.7 mm, and the measured elastic modulus was 18 kPa, as it came from the same gelatin batch as the 50 mm fat-simulating cube used in the previous experiment without lubrication.

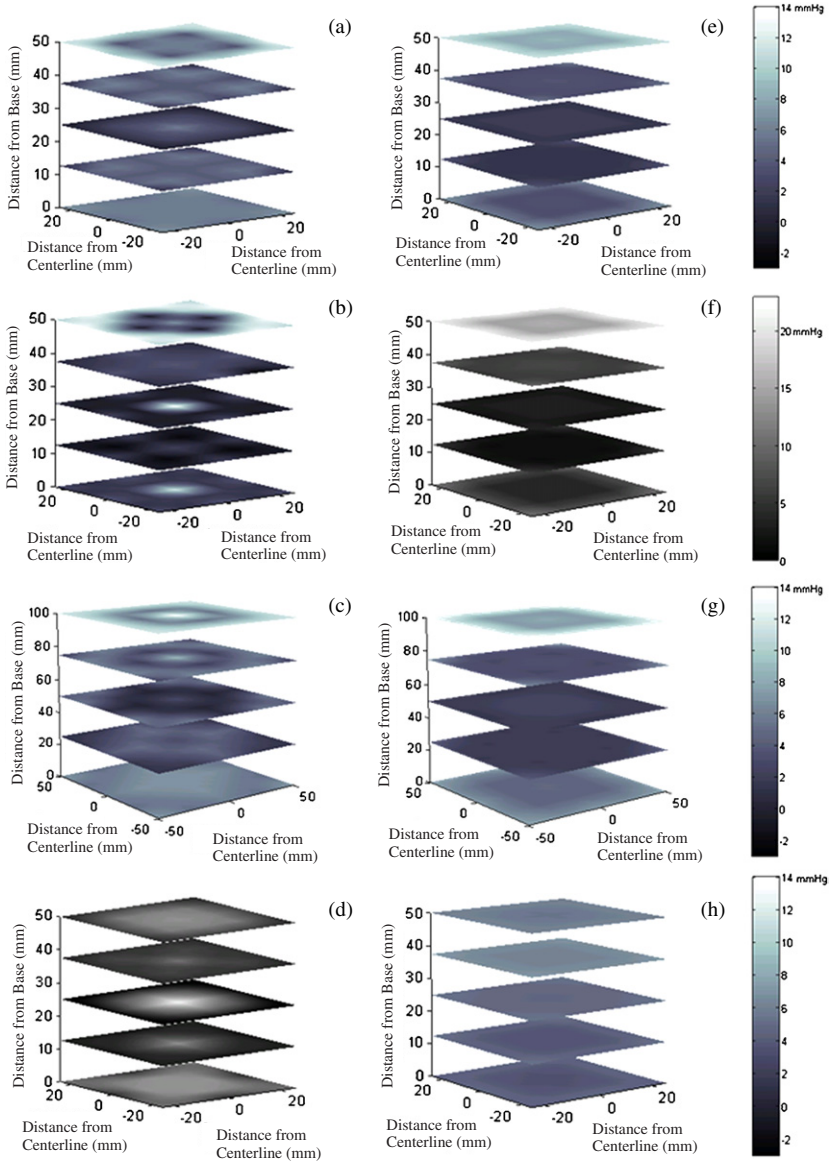

Figure 4. Maps of phantom (a)–(d) and corresponding FEA model pressure distributions (e)–(h). (a) and (e) show 50 mm adipose-simulating models without lubrication, (b) and (f) show 50 mm fibroglandular-simulating models without lubrication, (c) and (g) show 100 mm adipose-simulating models without lubrication, and (d) and (h) show 50 mm adipose-simulating models with lubrication.

When a 50 mm cube of fat-simulating gelatin was pressure mapped while using vegetable oil to reduce the shear forces on the upper and lower surfaces of the sample, the measured pressure distribution was very different. There were no observed high pressures at the periphery of the upper cube face, and there was greater symmetry along the z-axis. The point of highest pressure was the center of the cube, at 13 mmHg. The observed displacement was 4.9 mm, and the measured elastic modulus of the gelatin batch was 19.56 kPa. This did not match a

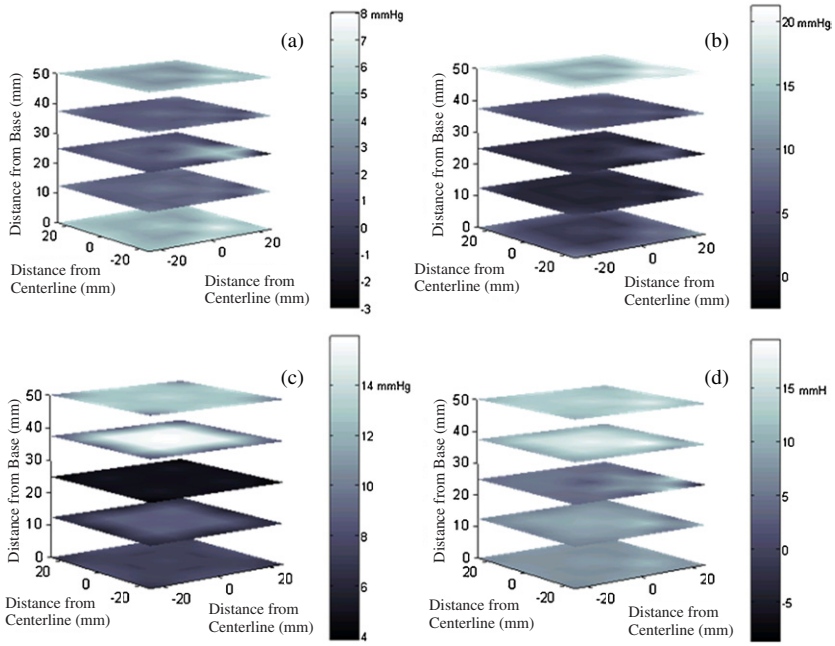

Figure 5. FEA pressure maps of heterogeneous material models including (a) an adipose model with a 93 kPa inclusion at 50% depth, (b) a fibroglandular model with a 93 kPa inclusion, (c) a composite with a 25 mm thick fibroglandular core and 12.5 mm adipose layer above and below, and (d) a similar composite with a 93 kPa inclusion.

FEA model with no surface shear stress, which displayed generally uniform internal pressures saved for the influence of gravity.

4.3. FEA pressure map of heterogeneous material models

The pressure distributions of the heterogeneous FEA models are displayed in figure 5, consisting of adipose-simulating material with a 93 kPa inclusion (upper left), fibroglandular-tissue-simulating material with a 93 kPa inclusion (upper right), a composite of adipose and fibroglandular material without an inclusion (lower left) and a similar composite with a 93 kPa inclusion (lower right). In all cases, the inclusion demonstrated higher pressures than the rest of the material at 50% depth. However, other effects were also observed: a high pressure signature on the surface of a model corresponding to the inclusion below and an increase in the pressure at tissue interfaces. As observed in the upper two samples of figure 5, a high point of pressure is present both above and below the inclusion in a straight line parallel to the vector of displacement. Another region of high pressure was observed in the adipose-fibroglandular composite, in which the highest pressures present were seen at the interface between the two materials, on the side of the less rigid of the two materials.

4.4. Pressure map planar averages by depth

Displayed in figure 6 are the z-axis planar pressure averages for the four phantom loading conditions (a), the corresponding FEA models (b), and the heterogeneous material FEA models (c). Figure 6(d) displays the pressure value at the center of each plane of the phantom, demonstrating patterns not observed in the FEA model centerpoints, figure 6(e). The planar

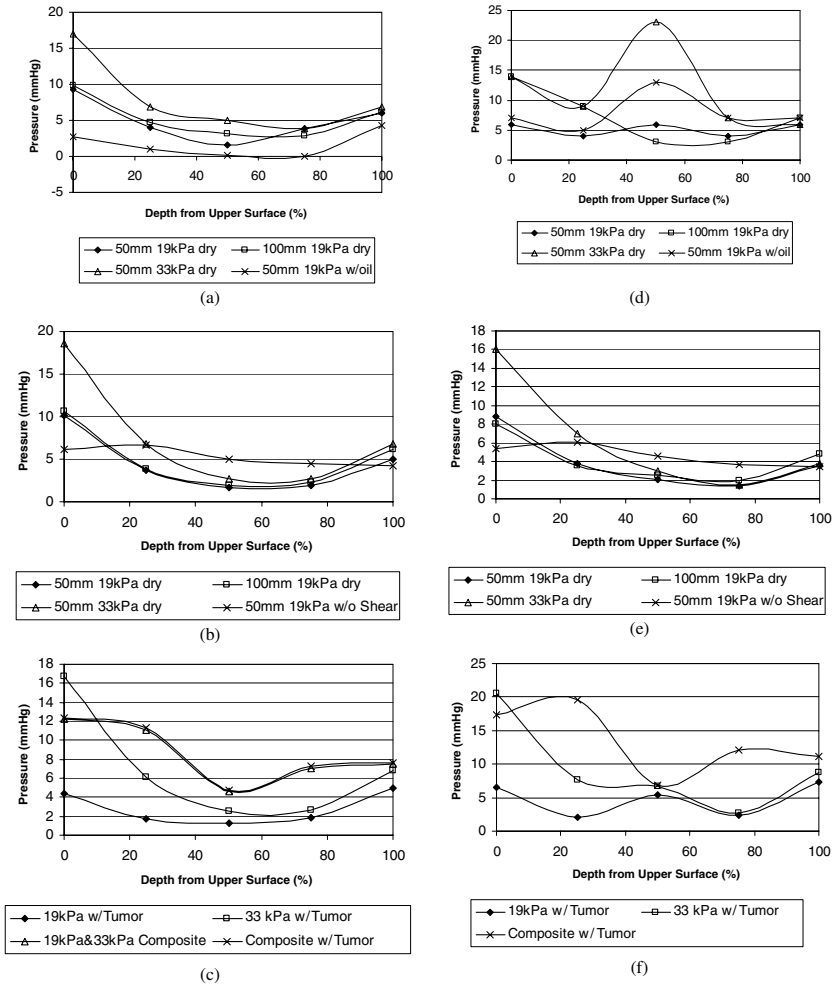

Figure 6. Left: the average planar pressures by depth for (a) phantom measurements, (b) homogenous material FEA models and (c) heterogeneous material FEA models. Right: the center point pressure in each plane for (d) the phantom measurements and (e) the homogenous FEA models. The graph at bottom right (f) displays the nodal pressures immediately above and below the tumor-like inclusion in the heterogeneous FEA models, with the inclusion at 50% depth.

pressure average graphs were generally concave, with higher pressures at the top and bottom of the sample, with a convergence towards 6 mmHg at the bottom surface. The planar averages of the FEA models with a surface shear stress showed close correlation, although the average pressure at 50% depth was somewhat lower, due to the lack of the high pressure centroid observed in three of the phantom samples. The lubricated sample did not correlate with the FEA model without a surface shear stress, indicating either that lubrication does not completely eliminate surface shear or that the pressure distribution in a lubricated phantom is dominated by nonlinear hyperelastic effects. For the heterogeneous FEA models, the presence of an inclusion was found to only affect the planar pressure distribution for the adipose-simulating material, where it reduced the pressure on the upper surface and increased the pressure around the tumor-like inclusion. The tumor pressures were found to be 5.4, 6.6 and 6.8 mmHg for the adipose, fibroglandular and composite models with inclusions respectively, a 414%, 258%

and 145% increase over the planar averages. Pressures directly above and below the tumor inclusion and within the tumor itself in the heterogeneous models are displayed in figure 6(f).

5. Discussion

It is clear from the experimental data that shear force, gravity, mechanical properties and sample geometry all contribute to complex heterogeneous pressure distribution within tissue-like constructs under pressure.

The influence of shear force is readily apparent in any of the mapped samples which were compressed without a vegetable oil lubricant. Without lubricant, the upper surface of the samples demonstrated a high internal fluid pressure along the edges of the sample, a high pressure which completely disappears in the lubricated sample. In this region of the lubricated sample, the gelatin was observed to displace a great deal, moving in relation to the steel compression plate. When there was no lubrication, the upper and lower surfaces of the sample showed little to no movement in the x and y directions due to static friction. While a fluid would deform without resistance under shear forces, and its pressure would not increase, the effectively linear elastic solid of the gelatin does resist the shear forces. This results in an increase in the hydrostatic pressure of the fluid inclusions within the solid. In the case of the experimental phantom, the fluid inclusion was a vegetable-oil-filled cavity in which the pressure transducer was inserted, but there is no reason to assume that this phenomenon would not translate to the micro- and nano-scale pores of tissue.

The phenomenon of shear-stress-induced fluid pressure is also important clinically, as it suggests that the location of highest pressure within a tissue will vary based upon the presence or absence of lubrication. As observed in the phantom data, absence of lubricant results in a higher pressure at the site where the pressure is applied. The upper surface average pressure of the fat-simulating cube without lubricant was roughly three times the average upper surface pressure of the fat-simulating cube with lubricant. The presence of lubricant also appears to move the peak pressure to the center of the sample within the z-axis, at least for samples of this geometry. The lack of correlation with the FEA model would seem to indicate that lubrication does not completely negate surface shear stress or that the pressure distribution in the lubricated sample is mostly due to nonlinear mechanical properties.

The profound effect of shear stress upon fluid pressures suggests that the skin may play a role in mitigating high subcutaneous IFP. It was observed by Reddy *et al* (1981) that subcutaneous IFP only reaches 65–75% of the externally applied pressure in a pig model. By contrast, the unlubricated phantoms in this study showed an average pressure of $\sim$100% or greater at the surface with local peaks of a significantly higher pressure. This suggests that pressure distribution may be lower in magnitude and perhaps more evenly distributed in clinical applications.

The effect of gravity was significant and would only grow more so in a clinical setting, such as in NIR imaging of breasts of different sizes. As can be observed in figure 6, the fluid pressure at the bottom surface of every phantom sample appeared to converge to approximately 6 mmHg, and the pressure at this level was much more evenly distributed than the upper level. In terms of loading conditions, the only difference between the upper and lower surfaces was that the lower surface was also subjected to body forces, the weight of the sample itself. In a sense, the gelatin cube, and tissue in general, is self-loading. In the case of the 50 mm cubes, the lower surface of the cube is exposed to 1.23 N, or 3.7 mmHg, that the upper surface is not. The 100 mm cube's lower surface was exposed to 7.4 mmHg more than the top. This body loading was not directly measured. Instead, change in pressure was measured when loading

was applied and then removed, as this made the pressure sensor reading more repeatable. Body loading, which is in place with or without compression, appears to affect the equilibrium pressure distribution of the samples under loading, making the pressure distribution at the lower levels more homogenous. In clinical applications, this might mean that a body part should be measured laterally rather than vertically with respect to gravity.

The role of the sample geometry is difficult to quantify, but there is clearly a change in pressure distribution between the samples of 50 and 100 mm in size. The 100 mm cube was the only sample that did not have a local pressure peak at the very center of the scaffold, perhaps indicating that the greater sample mass served to diffuse pressure more broadly, and the lower pressure per unit volume resulted in more linear elastic and less hyperelastic mechanical properties. In addition to sample dimensions, the presence of edges had a profound effect on pressure distribution at every level. On the upper and lower surfaces, edges and corners were the points of greatest shear-stress-contributed high pressures, while in the middle planes of the samples, the edges had the lowest pressures. Clearly, the much more complex geometries of biological structures and the large variety of scales are going to impact pressure distributions in a clinical setting.

Regional mechanical properties also play a strong role in IFP, as was suggested by both the homogenous phantoms and the heterogeneous models. Even in the homogenous phantoms, there is heterogeneity of stress distribution and therefore the heterogeneity of effective elastic modulus in this nonlinear material. This is a likely cause for the high centroid pressures observed in the phantoms. While the modulus variation in the homogenous samples is reasonably small for a practical range of applied pressure, the heterogeneous models possess a much greater difference in mechanical properties over a much more abrupt interface. This change is a nearly five-fold increase in elastic modulus between adipose and tumor tissues, for example. Sudden changes in material appear to lead to not only localized pressure peaks but also regions of higher pressure at the surface of a model above and below the inclusion. This is potentially clinically applicable, as it implies that any region of increased stiffness will cause pressure-related landmarks throughout the tissue when an external surface pressure is applied. Those changes could include a decreased microvascular volume, changes in scattering coefficient, and, if the localized pressure is sufficient to collapse microvessels, changes in the rate of local deoxygenation. These conclusions from the heterogeneous model data must be taken with caution, however, as the linear elastic model was found to be a poor predictor of pressure distribution at the centroid of homogenous phantoms. To validate this conclusion, a sophisticated nonlinear elastic model should be employed in the future.

6. Conclusions

Several conclusions can be drawn from this study with implications towards the use of applied external pressure, leading to an increase in IFP. The most obvious is that external pressure applied to the outside of a tissue-like material is not translated into a homogenous pressure distribution within the material. The interior fluid pressure will also be dependent upon the shear force contribution of the loading, the geometry of the material and the material's mechanical properties. Once this problem moves to the much more complex materials and geometries of human anatomy, it will likely be very difficult to predict pressure distribution at the range of 10 mmHg without knowing the effective elastic moduli and regional viscous coefficients, a task for which magnetic resonance elastography or ultrasound strain imaging might be appropriate. Any modality which can provide both internal displacement measurements and an estimate of regional mechanical properties possesses the potential to calculate internal fluid pressure distributions. The heterogeneous models suggest that a signal

change due to IFP will be of greater volume, and hence more detectable, than an inclusion itself. Other modalities, such as NIR diffused optical tomography, which can observe transient microvascular phenomena, could make use of these internal pressure variations to assist in diagnosis and treatment.

Numerous questions arise from this study. While IFP distribution based on an external loading of 10 mmHg appears heterogeneous in fat-simulating and fibroglandular-tissue-simulating tissue, higher pressures may result in a more uniform IFP distribution. For instance, microvascular pressure is in the order of 20 mmHg (Heldin *et al* 2004). If the goal is to occlude those vessels for near-infrared detection of deoxygenation, etc, applied pressures between microvascular pressure of 20 mmHg and systemic blood pressure should be investigated. Once these pressures are applied, however, the nonlinear nature of tissue mechanical properties may become even more relevant. As more force is exerted, more of the material stress–strain curve will become involved, and assuming a linear elastic model may be less appropriate. A future computational model of the system must include the nonlinear effective elastic modulus, which increases with increasing stress. Applying this model to real tissue would also require terms governing fluid migration, such as the vascular and lymphatic fluid terms in the poroelastic model. Creating such an all-inclusive model would be an important step towards practical clinical applications.

Acknowledgments

The authors wish to acknowledge the financial support of DOBI Medical International, Inc. and NIH grant no R33CA100984.

References

Azar F S, Metaxas D N and Schnall M D 2001 A deformable finite element model of the breast for predicting mechanical deformations under external perturbations *Acad. Radiol.* **8** 965–75

Barbour R L, Graber H L, Pei Y, Zhong S and Schmitz C H 2001 Optical tomographic imaging of dynamic features of dense-scattering media *JOSA A* **18** 3018–36

Bilston L E 2002 The effect of perfusion on soft tissue mechanical properties: a computational model *Comput. Methods Biomech. Biomed. Eng.* **5** 283–90

Boas D A and Dale A M 2005 Simulation study of magnetic resonance imaging-guided cortically constrained diffuse optical tomography of human brain function *Appl. Opt.* **44** 1957–68

Boucher Y and Jain R K 1992 Microvascular pressure is the principal driving force for interstitial hypertension in solid tumors: implications for vascular collapse *Cancer Res.* **52** 5110–4

Carp S A, Kauffman T, Fan Q, Rafferty E A, Moore R H, Kopan D B and Boas D A 2006 Compression-induced changes in the physiological state of the breast as observed through frequency domain photon migration measurements *J. Biol. Opt.* **11** 064016

Dehghani H, Doyley M M, Pogue B W, Jiang S, Geng J and Paulsen K D 2004 Breast deformation modelling for image reconstruction in near infrared optical tomography *Phys. Med. Biol* **49** 1131–45

Erkamp R Q, Skovoroda A R, Emelianov S Y and O'Donnell M 2004 Measuring the nonlinear elastic properties of tissue-like phantoms *IEEE Trans. Ultrason. Ferroelectr. Freq. Control* **51** 410–9

Gordon J E 1980 Biomechanics: the last stronghold of vitalism *Symposia for the Society of Experimental Biology: The Mechanical Properties of Biological Materials* (Cambridge: Cambridge University Press)

Greenleaf J F, Fatemi M and Insana M 2003 Selected methods for imaging elastic properties of biological tissues *Annu. Rev. Biomed. Eng.* **5** 57–78

Gutmann R, Leunig M, Feyh J, Goetz A E, Messmer K, Kastenbauer E and Jain R K 1992 Interstitial hypertension in head and neck tumors in patients: correlation with tumor size *Cancer Res.* **52** 1993–5

Guyton A C, Granger H J and Taylor A 1971 Interstitial fluid pressure *Physiol. Rev.* **51** 527–63

Heldin C H, Rubin K, Pietras K and Ostman A 2004 High interstitial fluid pressure—an obstacle in cancer therapy *Nat. Rev. Cancer* **4** 806–13

Jiang S, Pogue B W, Paulsen K D, Kogel C and Poplack S P 2003 *In vivo* near-infrared spectral detection of pressure-induced changes in breast tissue *Opt. Lett.* **28** 1212–4

Krouskop T A, Wheeler T M, Kallel F, Garra B S and Hall T 1998 Elastic moduli of breast and prostate tissues under compression *Ultrason. Imaging* **20** 260–74

Leiderman R, Barbone P E, Oberai A A and Bamber J C 2006 Coupling between elastic strain and interstitial flow: ramifications for poroelastic imaging *Phys. Med. Biol.* **51** 6291–313

Liu H T, Sun L Z, Wang G and Vannier M W 2003 Analytic modeling of breast elastography *Med. Phys.* **30** 2340–9

Nathan S S, DiResta G R, Casas-Ganem J E, Hoang B H, Sowers R, Yang R, Huvos A G, Gorlick R and Healey J H 2005 Elevated physiologic tumor pressure promotes proliferation and chemosensitivity in human osteosarcoma *Clinic. Cancer Res.* **11** 2389–97

Netti P A, Baxter L T, Boucher Y, Skalak R and Jain R K 1997 Macro- and microscopic fluid transport in living tissues: application to solid tumors *AIChe J. Bioeng. Food Nat. Prod.* **43** 818–34

Reddy N P, Palmieri V and Cochran G V 1981 Subcutaneous interstitial fluid pressure during external loading *Am. J. Physiol.* **240** R327–R329

Stokes G G 1845 On the theories of internal friction of fluids in motion *Trans. Camb. Phil. Soc.* **8** 287–305

Stur L E B, Reith A, Lepsøe S, Myklebust R, Wiig H and Reed R K 2003 Fluid pressure in human dermal fibroblast aggregates measured with micropipettes *Am. J. Physiol. Cell Physiol.* **285** C1101–C1108

White F M 1991 *Viscous Fluid Flow* (Boston, MA: McGraw Hill)